Optimal Multi-Site Selection for a PV-based Lunar Settlement Based on A Novel Method to Estimate Sun Illumination Profiles

Raya-Armenta, José Maurilio; Bazmohammadi, Najmeh; Saha, Diptish; Vasquez, Juan C.; Guerrero, Josep M.

Published in:
Advances in Space Research

DOI (link to publication from Publisher):
10.1016/j.asr.2022.12.048

Publication date:
2023

Document Version
Publisher's PDF, also known as Version of record

Citation for published version (APA):
Raya-Armenta, J. M., Bazmohammadi, N., Saha, D., Vasquez, J. C., & Guerrero, J. M. (2023). Optimal Multi-Site Selection for a PV-based Lunar Settlement Based on A Novel Method to Estimate Sun Illumination Profiles. *Advances in Space Research*, *71*(5), 2059-2074. https://doi.org/10.1016/j.asr.2022.12.048

Available online at www.sciencedirect.com

ScienceDirect

Advances in Space Research 71 (2023) 2059–2074

ADVANCES IN SPACE RESEARCH
(a COSPAR publication)

www.elsevier.com/locate/asr

Optimal multi-site selection for a PV-based lunar settlement based on a novel method to estimate sun illumination profiles

José Maurilio Raya Armenta *, Najmeh Bazmohammadi, Diptish Saha, Juan C. Vasquez
Josep M. Guerrero

Center for Research on Microgrids (CROM), AAU Energy, Aalborg University, Aalborg East 9220, Denmark

Received 30 May 2022; received in revised form 16 December 2022; accepted 25 December 2022
Available online 2 January 2023

Abstract

Recently, space organizations have considered the Moon to host lunar bases. Such bases require power and energy to function. However, the efficient and safe use of the energy resources on the Moon is a huge challenge. Space photovoltaic (PV) power systems are appealing technologies due to their maturity and high solar energy availability at some locations on the Moon. The effectiveness of these PV systems depends on their selenographic location, which might necessitate the deployment of energy storage technologies to cover the base's energy demand. Some analysts have proposed the installation of PV modules on kilometers-tall towers near the lunar poles to harvest more solar energy and limit the need for energy storage systems (ESSs). Alternatively, this paper proposes to harvest the energy from multiple sites in the lunar South Pole region using a novel technique to compute the Sun illumination profile and the LOLA topographic databases to compute the terrain elevations. The proposed algorithm seeks the most optimal configuration of sites and tower heights to minimize the longest night period and total distance between the sites. This study assesses groups of 1 to 6 sites assuming the use of towers having heights of 10, 100, and 500 [m]. The time horizon for the analysis is one Axial Precession Cycle, which is approximately 18.6 years. According to the results, a system of two sites with a separation of 42.05 [km] and towers of 500 [m] height has a maximum darkness period of only 3 [h] while another solution proposes a system of three sites with towers of 10 [m] that removes the need of EES (solar eclipse periods by the Earth are not considered). The proposed technique is suitable for engineering applications, such as base planning and operation management.

Keywords: Space microgrid; Moon; Optimal allocation; Time-series illumination profile; LOLA; DEM

1. Introduction

Over the past few years, various space organizations such as the National Aeronautics and Space Administration (NASA), Japan Aerospace Exploration Agency (JAXA), and China National Space Administration (CNSA) have scheduled several missions to the Moon to build a lunar base (Dunbar, 2021; JAXA, 2019). Establishing a human base on the Moon requires a complete electrical system infrastructure consisting of power generation, transmission, and distribution as well as an energy storage system (ESS). A high level of reliability, resiliency, robustness, optimality,and stability (RRROS) is compulsory. In this regard, the concept of microgrids (MGs) could be a potential solution given the wealth of experience from terrestrial applications. However, the outer space harsh operating conditions will heavily challenge the MGs in terms of RRROS, and the RRROS depends largely on the level of technology used. Such specific requirements have coined

* Corresponding author.
E-mail addresses: mauriliorarm78@gmail.com (J.M. Raya Armenta), naj@energy.aau.dk (N. Bazmohammadi), dsa@energy.aau.dk (D. Saha), juq@energy.aau.dk (J.C. Vasquez), joz@energy.aau.dk (J.M. Guerrero).

https://doi.org/10.1016/j.asr.2022.12.048
0273-1177/© 2023 COSPAR. Published by Elsevier B.V.

the term space microgrids (SMGs). Regarding energy generation for space applications, solar photovoltaic (PV) systems, nuclear fission-based reactors (Colozza, 2020; Gibson and Schmitz, 2020), and electrostatic charge from the lunar regolith have been proposed (Choi et al., 2010). Nuclear fission-based reactors are modular, small in mass and volume, and can generate power independent of the site location and the illumination conditions. However, appropriate shielding is required and the reactors must be placed at a distance from the lunar base to reduce the crew's exposure to nuclear radiation (Colozza, 2020). At the end of the reactor lifetime it will be deactivated until the radiation levels diminish to safe levels for human access/handling and then either remain in place or moved to a less trafficked location (Bukszpan, 2020). Solar PV systems can be placed near the lunar base, allow easy expansion, and are a tried and well-tested technology in space applications without requiring additional heavy infrastructure. The absence of atmosphere on the Moon makes solar power the most abundant source of energy due to the unobstructed and non-diffused reception of solar irradiation on the lunar surface. PV systems on the Moon are exposed to micrometeorites, extreme temperature cycles, deep vacuum, intense electrostatic fields (The intense electrostatic fields can charge the coverglass of PV-cells and it may cause permanent damage to the array components through undesired discharges (Lisbona, 2005)), ultraviolet (UV) radiation, nuclei/ion particle radiation, and galactic cosmic rays (GCRs) to a lesser extend (Lisbona, 2005; Raya-Armenta et al., 2021; Masayuki et al., 2020; Peng et al., 2020). All these conditions will demand a careful design of the entire power system.

In general, non-polar lunar latitudes are continuously illuminated for ~ 15 days followed by ~ 15 days of continuous darkness. Unlike non-polar latitudes, some high terrain locations near the lunar South Pole have uninterrupted sunlight for six months with frequent illumination-darkness cycles over the other six months (Fincannon, 2008a; Freeh, 2009; Fincannon, 2020), which makes the integration of accurately-sized ESSs a necessity. Nonetheless, the ESSs represent a significant challenge in terms of volume, weight, and high lifetime degradation rates. By installing the solar panels on high towers, terrain shadows effects can be reduced and possibly eliminated resulting in a reduction of the ESS size (Fincannon, 2007; Fincannon, 2008a). Although lunar polar regions are more appealing for a lunar base, the low elevation angle of the Sun and the high terrain elevations can result in long shadows of hundreds of kilometers across the lunar surface possibly covering the base (Fincannon, 2007; Fincannon, 2008b; Fincannon, 2008a; Li et al., 2008). Illumination conditions of the lunar polar regions have been analyzed using the digital elevation models (DEMs) provided by the Earth-based radar and the *Clementine* spacecraft imagery in (Fincannon, 2007; Fincannon, 2008a; Fincannon, 2008b). In (Noda et al., 2008), the authors create the lunar DEM from the laser altimeter on the *KAGUYA* spacecraft and identify several highly illuminated and permanently shadowed locations on the Moon. A theoretical study is presented in (Li et al., 2008) to estimate the solar illumination on the Moon using the selenographic longitude and latitude, the dimensionless distance between the Sun and the Moon relative to 1 astronomical unit (AU) and comparing the lunar elevations in solar irradiance direction within 210 km. The high-resolution altimetry data from the Lunar Orbiter Laser Altimeter (LOLA) on the Lunar Reconnaissance Orbiter (LRO) is used in (Mazarico et al., 2011) to assess the illumination of lunar polar areas. The most illuminated locations near both polar regions, the extent of permanently shadowed regions (PSRs), and scattered light received by the PSRs are identified. Furthermore, in (Speyerer and Robinson, 2013), high-resolution images of the lunar polar regions provided by the Lunar Reconnaissance Orbiter Camera (LROC) are used to identify permanently illuminated lunar polar regions.

Several studies have presented highly illuminated places for future lunar bases and some have discussed the combination of different sites to increase the energy availability (Bussey et al., 1999; Fincannon, 2007). However, an optimization method to select the best locations aiming to reduce the distance between sites and the night time periods has not been discussed yet. In this sense, this paper proposes to find the optimal combination between different sites at different tower heights to reduce darkness periods while keeping a short distance between the individual locations. By considering a multi-site structure (such as in terrestrial multi-microgrids (MMGs)) for the lunar power system, the level of RRROS will naturally increase by relying on more than one location to harvest the solar energy while the height of the PV structures will reduce considerably. The results show that setting up two interconnected sites at 291.7803° longitude, −88.6704° latitude, and 197.7447° longitude, −89.6884° latitude, with a tower height of 500 $[m]$ each, the longest darkness time will be around 3 $[h]$ and the separation is 42.05 $[km]$ between the sites. The need of any ESS can be completely removed (except for the eclipse of the Sun by Earth) with a three-site configuration, one at 123.7604° longitude, −88.8084° latitude, another at 222.5634° longitude, −89.4734° latitude, and a third one at 291.5466° longitude, −88.6782° latitude, with a tower height of 10 $[m]$ each. Nonetheless, for this case, the separation between the sites is about 158.8 $[km]$. Such large distances might potentially be covered in the near future with new power transmission technologies such as laser wireless power transmission, which is currently under investigation (Jin and Zhou, 2019; Kerslake, 2008; Summerer and Purcell, 2009).

In order to identify highly-illuminated areas on the Moon for installing PV systems and establishing a lunar base, knowledge of the solar illumination profile is required. Efficient control and operation management of a lunar power system needs an estimation of available solar power with sufficient accuracy. In this regard, this paper also proposes a novel technique to estimate the Sun illumination time-series profiles on the lunar poles using the LOLA DEMs for engineering purposes. The proposed technique utilizes the lunar topographic information to estimate the critical elevation angles and find the approximate Sun position in the sky of the Moon using analytical models that are solved numerically. The Sun availability is then determined by comparing the estimated Sun elevation angle with critical elevation angles. The average illumination profile is computed using the proposed method and compared with an existing technique that shows a good agreement on the results. The identified trajectory of the Sun is compared with the results provided by the Horizons System of NASA showing a good agreement.

The rest of the paper is organized as follows. Computation of the Moon topography is presented in Section 2. Section 3 is dedicated to the estimation of the Sun elevation. In Section 4, the Sun illumination time-series profiles, initial conditions, and validations are provided. The site selection procedure is presented in Section 5 and the simulation results are discussed in Section 6. Finally, conclusions are provided in Section 7.

2. The topography of the lunar south pole

One of the essential requirements of estimating the solar irradiation profile at a specific location on the Moon's polar region, is having knowledge of the Moon's topography. Recently, the data set being provided by the LOLA device installed in the LRO has shown the highest resolution. The spatial resolutions reported during the year 2010 were ~ 10 $[m]$ and ~ 50 $[m]$ in radial (R) and along-track (S) directions, respectively (Smith et al., 2010b). The resolution in cross-track (W) direction was approximately 0.04^o, corresponding to ~ 1.2 $[km]$ at the equator and ~ 200 [m] at $\pm 80^o$ latitude after one year of its lunch in 2010 (Smith et al., 2010a). This is because the resolutions depend on the number of orbits that the LRO travels around the Moon (with an orbital period of around 112–114 min). The data is generated by means of a laser diffracted in five parts, each having a coverage area with a diameter of approximately five meters on the Moon surface. The spacecraft has a nominal orbit of 50 $[km]$, a nominal ground track speed of 1600 $[m/s]$, and a shutting frequency of around 28 $[Hz]$, resulting in 140 measurements per second, see Fig. 1 (Neumann et al., 2016; Smith et al., 2010b). However, the valid measurements are in the range of 80 to 90 measurements per second (Smith et al., 2010b). Ideally, considering the round trip time of the light beams (LRO-Moon-LRO), the LOLA receivers should have a precision of approximately 9 $[cm]$. However, in practice, the highest precision achieved is ~ 12 $[cm]$ (Smith et al., 2010b). These data have helped to find the deepest place on the Moon located in the *"Antoniadi crater"* at -9.117 $[km]$ (187.5074^o E, 70.360^o S) with respect to a reference lunar radius of 1737.4 $[km]$. The highest elevation has been located at about 10.7834 $[km]$ (201.378^o E, 5.401^o N) with the same reference (Neumann et al., 2016; Smith et al., 2010b; Smith et al., 2010a). The data from LOLA is organized as both raw and derived data (NASA, 2020). The derived gridded data record (GDR), which is a DEM of the Moon surface elevations with respect to the reference of lunar average radius, in polar stereographic projection is used in this study, see Table 1. This data set is formatted as binary images with 16-bit integers (Neumann et al., 2016; Smith et al., 2010a), and the transformation to meter is calculated as follows,

$$h = (DV)(SF) + R, \tag{1}$$

where h is the elevation $[m], DV$ is the digital value in $[m], SF = 0.5$ is the scaling factor, and $R = 1737400$ $[m]$ is the offset or average lunar radius.

Considering the data in the form of a table, see Fig. 2, the top-left corner is the origin of the projected data (polar

Table 1
Information of the DEM used in this study (GDR). The dataset provides the height at each location based on an average between the number of measurements at the specific location. It should be noticed that the actual error in height is unknown.

File name: ldem_75s_120m.img		
Variable	**Symbol**	**Value**
Resolution	a	0.120 $[km/pixel]$
	r_{pix}	252.695 $[pixel/deg]$
SF	SF	0.5

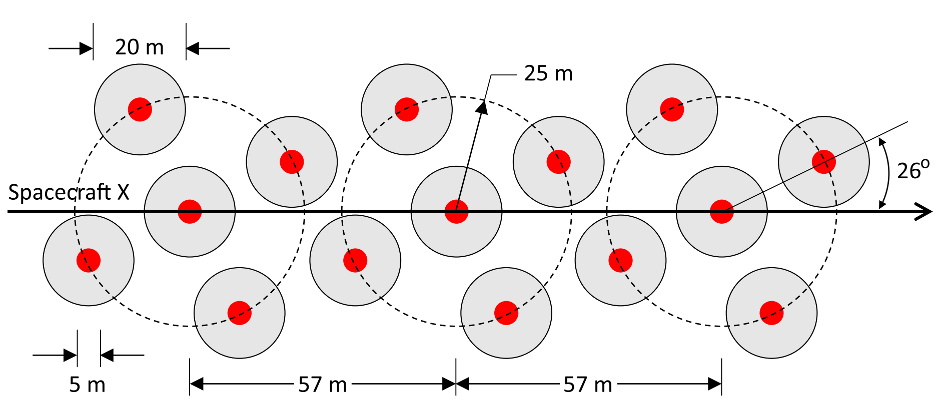

Fig. 1. LOLA pattern upon the lunar surface. Adapted from (Neumann et al., 2016).

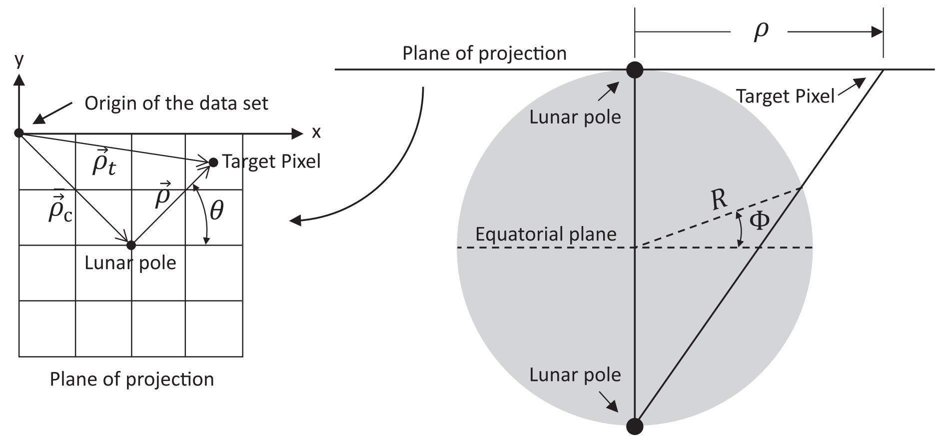

Fig. 2. Polar stereographic projection of the data. The polar stereographic projection (2D projection) is assumed to be a parallel plane in $z = \pm R/2$ with respect to the equatorial plane in $z = 0$, the sign depends on the pole of projection.

stereographic projection) and the center of the table represents the lunar pole. Thereby, a data point (target pixel) with the origin at the center of the table is given as

$$\vec{\rho} = \vec{\rho}_t - \vec{\rho}_c, \tag{2}$$

where $\vec{\rho}_t$ and $\vec{\rho}_c$ are the polar vector position of the target pixel and the lunar pole, respectively, both with origin at the top-left corner. The latitude and longitude of each pixel are expressed as following, see Fig. 2.

$$\Phi = \left[\frac{\pi}{2} - 2\arctan\left(\frac{\rho}{2R}\right)\right]\alpha_{ls} \rightarrow \text{latitude}, \tag{3}$$

$$\theta_l = \frac{\pi}{2} - \theta \rightarrow \text{longitude}, \tag{4}$$

where α_{ls} is the latitude sign being 1 for the north pole and -1 for the south pole and θ is the angle shown in Fig. 2.

Taking into account that each pixel provides the terrain elevation with respect to R in that specific point, the spherical coordinate of each point of terrain with origin at the center of the Moon is expressed as

$$\vec{r} = r_x\hat{x} + r_y\hat{y} + r_z\hat{z}, \tag{5}$$

where $r_x = |\vec{r}|\sin(\phi)\cos(\alpha_{ls}\theta), r_y = |\vec{r}|\sin(\phi)\sin(\alpha_{ls}\theta)$, $r_z = |\vec{r}|\cos(\phi), |\vec{r}| = R + h$, and $\phi = \frac{\pi}{2} - \Phi$. The position of the point-of-interest (POI) in the projected array of data with origin at the pole (see Fig. 2) is obtained as,

$$\vec{\rho}_0 = |\vec{\rho}_0|\left[\vec{i}\cos\theta_0 + \vec{j}\sin\theta_0\right], \tag{6}$$

$$|\vec{\rho}_0| = \left|\frac{\pi}{2}\alpha_{ls} - \Phi_0\right| r_{pix}a, \tag{7}$$

$$\theta_0 = \frac{\pi}{2} - \theta_{l,0}, \tag{8}$$

where the subscript 0 refers to the POI and r_{pix} and a are resolutions of the data in $[pixel/deg]$ and $[distance/pixel]$, respectively, see Table 1. The value of $|\vec{\rho}_0|$ in pixels is obtained by removing a. Since the *critical angles* (the critical angle is the largest angle formed by the horizon of an observer located on the POI and the terrain elevations observed from the POI in a specific direction, see Fig. 4) in a specific position is sought, all the data points should be referenced to a new origin at the POI. This can be achieved by

$$\vec{\rho}_p = \vec{\rho} - \vec{\rho}_0, \tag{9}$$

where $\vec{\rho}_p$ represents the vector pointing to each pixel in the data set with origin at the POI.

Four unitary vectors $\hat{\rho}_A, \hat{\rho}_B, \hat{\rho}_C$, and $\hat{\rho}_D$ (one for each corner of the pixel) are formed for each point of the data set, see Fig. 3. The vectors for each corner, with origin in the POI, are expressed as

$$\vec{\rho}_C = \vec{\rho}_p - \frac{a}{2}(\hat{i} - \hat{j}), \vec{\rho}_B = \vec{\rho}_p + \frac{a}{2}(\hat{i} + \hat{j}), \tag{10}$$
$$\vec{\rho}_D = \vec{\rho}_p - \frac{a}{2}(\hat{i} + \hat{j}), \vec{\rho}_A = \vec{\rho}_p + \frac{a}{2}(\hat{i} - \hat{j}).$$

Then, a cross-product is applied between the unitary vectors of (10), of each pixel, and its corresponding location vector $\vec{\rho}_p$ to estimate the maximum and minimum (negative with the largest value) distances between $\vec{\rho}_p$ and the unitary vectors, as follows (see Fig. 3)

$$l_{max} = \max\left(\left\{\vec{\rho}_p \times \hat{\rho}_x : x = A, B, C, D\right\}\right), \tag{11}$$

$$l_{min} = \min\left(\left\{\vec{\rho}_p \times \hat{\rho}_x : x = A, B, C, D\right\}\right). \tag{12}$$

Therefore, if the distance between the vector of each pixel, $\vec{\rho}_p$, and a projection of the Sun position in the stereographic projection plane, $\vec{\rho}_s$, is between l_{min} and l_{max}, this means that this pixel is between the POI and the Sun, which might be the elevation corresponding to the critical angle. The distance is determined by

$$\vec{l} = \vec{\rho}_p \times \hat{\rho}_s, \tag{13}$$

while the pixels in the opposite direction to the Sun are ignored by applying the condition $\vec{\rho}_p \cdot \hat{\rho}_s > 0$.

The estimation of the critical angle in the direction of the Sun is thereby given as

$$\beta_{crit} = \frac{\pi}{2} - \min\left\{\arccos\left[\frac{\vec{r}_0 \cdot (\vec{r} - \vec{r}_0)}{|\vec{r}_0||\vec{r} - \vec{r}_0|}\right]\right\}, \tag{14}$$

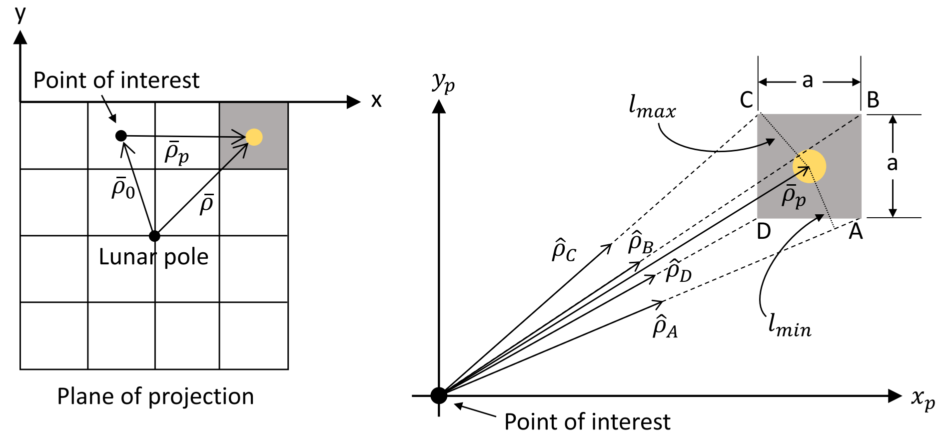

Fig. 3. Shifting reference frame from the pole to the POI. Unitary vectors corresponding to the corners of each pixel in the data set. The origin is in the POI.

where $\vec{r}$ and $\vec{r}_0$ are the spherical vectors of the target pixel and the POI, respectively, see Fig. 4.

3. The Sun elevation in the lunar sky

The location of the Sun in the Moon's sky has been estimated based on the numerical solution of the *three-body problem*, represented by the Sun-Earth-Moon system (see Fig. 5), using the Newton's gravitation law given below. It should be noticed that the computation of the Sun position in the lunar sky can be obtained directly from the Ephemerides database[1]. However, one of the contributions of this study is a new method to estimate the Sun location from any point of the Moon for engineering purposes.

$$\vec{F}_n = \sum_{k=1}^{N} G m_n m_k \frac{\vec{R}_k - \vec{R}_n}{\left|\vec{R}_k - \vec{R}_n\right|^3}, k \neq n \tag{15}$$

where $\vec{F}_n$ is the total force upon the body n, having mass m_n, due to the action of other $N-1$ bodies with mass of $\{m_k : k \in 1, \ldots, N, k \neq n\}$ (assuming a closed system with N bodies), $N = 3$ is the total number of bodies, $G \approx 6.67408 \times 10^{-11}$ $[m^3/kg - s^2]$ is the gravitational constant, and $\vec{R}_n$ and $\vec{R}_k$ are the radius-vector to the center of mass (CM) of bodies n and k, respectively, with origin at the system's barycenter, see Table 3. Thereby, the total force upon each individual body can be computed.

The linear momentum and displacements of each individual are numerically estimated using the Euler method as follows.

$$\vec{p}_{n,k} = \vec{p}_{n,k-1} + \vec{F}_{n,k}\Delta t, n = 1, \ldots, N, (16)$$

$$\vec{R}_{n,k} = \vec{R}_{n,k-1} + \frac{\vec{p}_{n,k}}{m_n}\Delta t, n = 1, \ldots, N, (17)$$

[1] Ephemerides - Horizons web interface, Jet Propulsion Laboratory (JPL), NASA (NASA-JPL, 2021), https://ssd.jpl.nasa.gov/horizons/app.html#/.

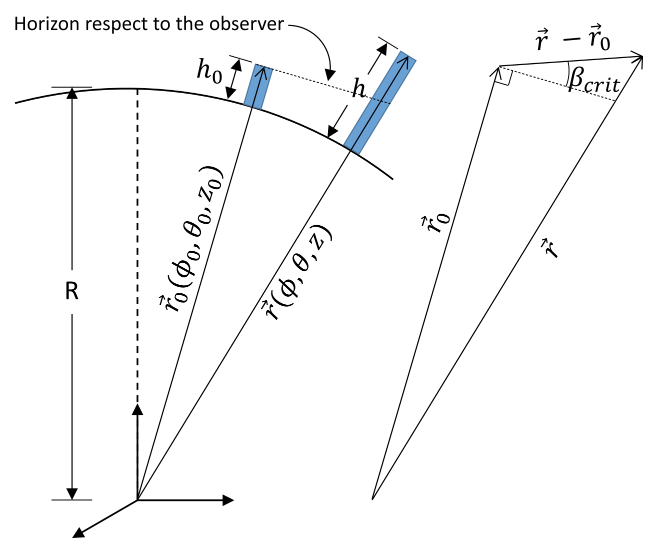

Fig. 4. Spherical vectors corresponding to the POI and an arbitrary point (target pixel) with elevation of h. The critical angle is measured between the horizon of the observer and the difference vector of the POI and the elevation vector of the arbitrary point.

where $\vec{p}_n$ and $\vec{F}_n$ are the linear momentum and the force upon the body n, respectively, and Δt is a small time step. The subscripts k and $k-1$ indicate the current and the previous time steps, respectively.

The radius vector that connects the Sun's CM with the location of the POI, $\vec{R}_{Sl}$, is used to compute the Sun elevation. The Sun is assumed to be a disk with a constant average diameter of about 0.5329 degrees in the lunar sky. This vector is expressed as

$$\vec{R}_{Sl} = \vec{R}_{SM} + \vec{r}_{cl}, \tag{18}$$

where $\vec{r}_{cl}$ is the vector connecting the Moon's CM with the location of the POI, see Fig. 6. First, vector $\vec{r}_{cl}$ is expressed in a reference frame aligned to the lunar pole and the equatorial plane (polar reference frame), see Fig. 6, such as

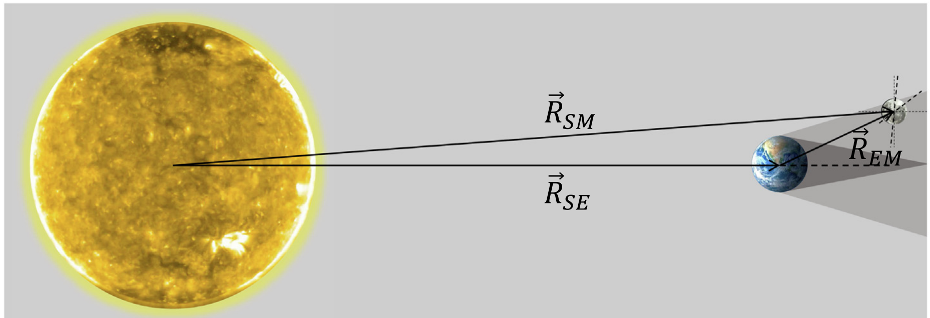

Fig. 5. Graphical representation of the Sun-Earth-Moon system. The figure is not drawn to scale.

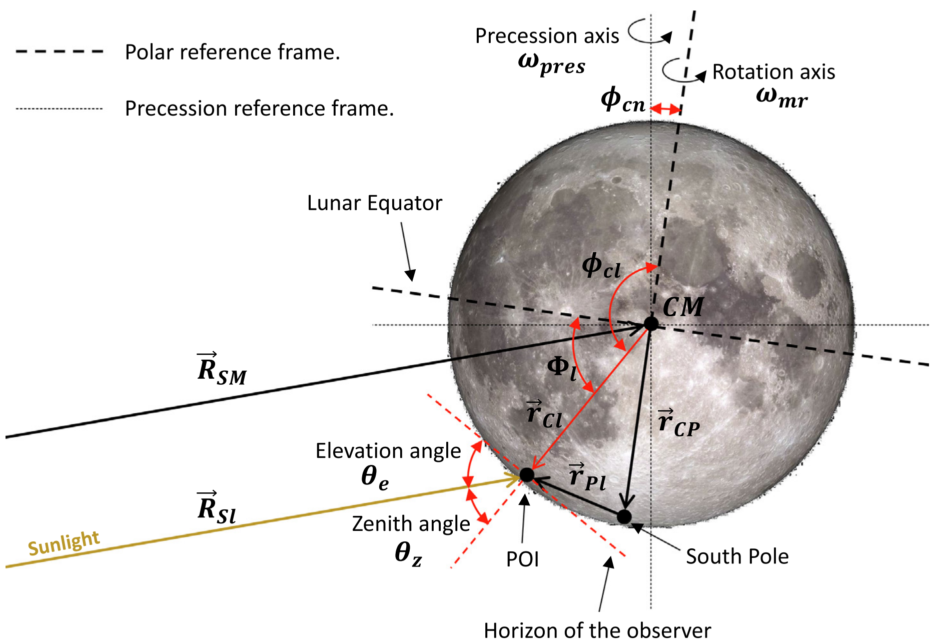

Fig. 6. Graphical representation of the location of the POI over the south pole of the Moon. The figure is not at scale.

$$\vec{r}_{cl,d} = \vec{r}_{cl,x}\hat{i} + \vec{r}_{cl,y}\hat{j} + \vec{r}_{cl,z}\hat{k}, \tag{19}$$

where $\vec{r}_{cl,x} = |\vec{r}_{cl}|\sin\phi_{cl}\cos\theta_{cl}, \vec{r}_{cl,y} = |\vec{r}_{cl}|\sin\phi_{cl}\sin\theta_{cl}, \vec{r}_{cl,z} = |\vec{r}_{cl}|\cos\phi_{cl}$, and $|\vec{r}_{cl}| = R + h$. The angles are expressed as

$$\phi_{cl} = \frac{\pi}{2} - \Phi_l, (20)$$

$$\theta_{cl} = \omega_{mr}t + \theta_{cl,0}, (21)$$

where ϕ_{cl} is the angle between the North Pole, CM, and POI. The latitude of the POI is Φ_l. The angle of rotation and the spin velocity of the Moon in its own axis are represented as θ_{cl} and ω_{mr}, respectively. $\theta_{cl,0}$ is the initial condition of the angle of rotation, see Table 3. Since the Moon is tidally locked to Earth, the Moon's spin and rotation velocities are in average the same, so ω_{mr} might be approximated to

$$\omega_{mr} = \frac{|\vec{v}_{EM}|}{|\vec{R}_{EM}|}, \tag{22}$$

where $\vec{v}_{EM}$ is the tangential velocity of the Moon around Earth while $\vec{R}_{EM}$ is the relative radius vector between them, see Fig. 5.

Then, $\vec{r}_{cl,d}$ in (19) has to be transformed from the polar reference frame to the precession reference frame to include the effect of the precession period (the Axial Precession Cycle (APC) is the time that the Moon's north pole describes a small circle in the constellation Draco), see Fig. 6 and Fig. 7. The transformation may be performed as follows

$$\vec{r}_{cl} = T_{d,s}\vec{r}_{cl,d}, \tag{23}$$

$$T_{d,s} = \begin{bmatrix} \cos\theta_{cn} & -\cos\phi_{cn}\sin\theta_{cn} & -\sin\phi_{cn}\sin\theta_{cn} \\ \sin\theta_{cn} & \cos\phi_{cn}\cos\theta_{cn} & \sin\phi_{cn}\cos\theta_{cn} \\ 0 & -\sin\phi_{cn} & \cos\phi_{cn} \end{bmatrix},$$

where ϕ_{cn} is the obliquity to the ecliptic, see Table 3. The variable θ_{cn} is the rotational angle due to the precession period and is expressed as

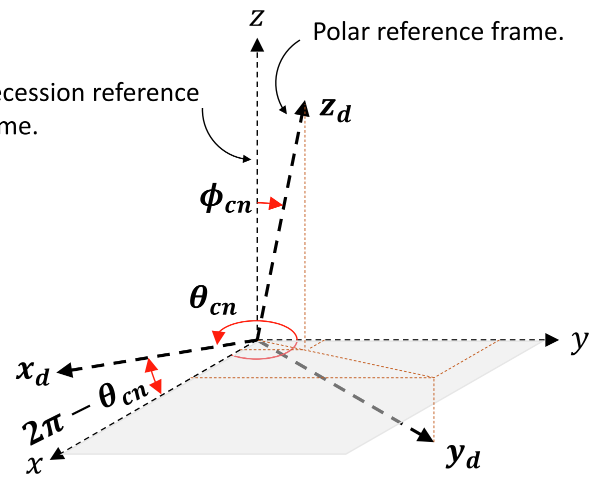

Fig. 7. Reference frames for transformation from polar to precession reference frame.

$$\theta_{cn} = -\omega_{pres}t + \theta_{cn,0} \tag{24}$$

where ω_{pres} is the angular precession velocity and $\theta_{cn,0}$ shows the initial position of the lunar axis, which is initially adjusted with data provided by the JPL[10], see Fig. 7 and Table 3. The negative sign is because the APC turns clockwise (westwards) when viewed from the celestial north.

The zenith angle, θ_z, and the elevation angle, θ_e, can be computed from the dot product between $\overrightarrow{R}_{sl}$ and $\overrightarrow{r}_{cl}$ as follows, see Fig. 6,

$$\theta_e = \frac{\pi}{2} - \theta_z, \tag{25}$$

$$\theta_z = \arccos\left(-\frac{\overrightarrow{R}_{sl} \cdot \overrightarrow{r}_{cl}}{|\overrightarrow{R}_{sl}||\overrightarrow{r}_{cl}|}\right). \tag{26}$$

The values of the physical parameters are summarized in Table 2 and the main assumptions in Table 3.

4. The time-series illumination profiles, initial conditions, and validations

In this paper, the worst lunar day (WLD) in an APC (≈18.6 years), for a single site, is assumed to be the day with the largest average value of the total number of hours in darkness and the longest period of darkness. Even though close locations upon the south pole of the Moon might have the same WLD, the topography of the lunar terrain hugely impacts the availability of solar energy at each spot. In this respect, several papers have presented the illumination conditions of the lunar poles to estimate the potential for solar energy harvesting, (Barker et al., 2021; Fincannon, 2007; Fincannon, 2008b; Fincannon, 2008a; Mazarico et al., 2011; Speyerer and Robinson, 2013).

For this study, twenty sites previously identified in (Mazarico et al., 2011) have been selected and presented in Table 4, see Fig. 14. Then, a search of the highest elevation around each position was carried out to find an adjusted location. The last column of Table 4 provides the absolute error of the average illumination in the reported and adjusted positions. The error between the two databases can stem from different sources as listed below.

- The reported database belongs to July-2009 to February-2010 whereas the dataset used for this study is updated up to February-2017.
- The resolution of the database is 240 [m] (square pixels) whereas for this study it is 120 [m].
- The shape of the lunar terrain between two samples is found by linear interpolation in the database whereas in this study it is considered to be constant (this mainly produces the big difference in Site 19).
- Different models for the Sun location in the lunar sky and Moon orientation are used.
- Average values are calculated for four precession cycles from 1970 to 2044 whereas this study calculates the average value for one precession cycle from 2023 to 2042.

The computed Sun trajectory (the center of the solar disk) has been compared with the results provided by the Horizons System of the JPL of NASA (NASA-JPL, 2021)[10], which are assumed to be a reference for the solution, and similar results have been obtained for all the sites.

Table 2
Physical values and bases of the parameters used in this study (Williams, 2020a; Williams, 2020b; Williams, 2018). Sun data: https://nssdc.gsfc.nasa.gov/planetary/factsheet/sunfact.html, Earth data: https://nssdc.gsfc.nasa.gov/planetary/factsheet/earthfact.html, Moon data: https://nssdc.gsfc.nasa.gov/planetary/factsheet/moonfact.html.

Body	Parameter	Value	Units
Sun	Mass	1988500×10^{24}	$[kg]$
	Sidereal year	365.256	$[days]$
	Av. Distance to Earth	1	$[AU]^*$
Earth	Mass	5.9724×10^{24}	$[kg]$
	Aphelion	152.099×10^9	$[m]$
	Perihelion	147.092×10^9	$[m]$
	Min. orbital velocity	29290	$[m/s]$
Moon	Mass	7.346×10^{22}	$[kg]$
	Apogee	0.4055×10^9	$[m]$
	Perigee	0.3633×10^9	$[m]$
	Orbit inclination	5.145	$[^o]$
	Obliquity to Ecliptic (ϕ_{cn})	1.535	$[^o]$
	Axial precession	18.6	$[yrs]$
	Average radius, R	1737.4×10^3	$[m]$
	Max. orbital velocity	1082	$[m/s]$
	Sidereal period	27.3217	$[days]$
	Synodic period	29.53	$[days]$
	Av. spin vel. (ω_{mr})	$\frac{2\pi}{27.3217\times24\times3600}$	$[rad/s]$
	Precession ang. vel. (ω_{pres})	$\frac{2\pi}{18.6\times365.242\times24\times3600}$	$[rad/s]$
Bases	Mass	1988500×10^{24}	$[kg]$
	Time	$365.256 \times 24 \times 3600$	$[s]$
	Distance	149597870.7×10^3	$[m]$

* 1 AU is 149597870.7×10^3 $[m]$.

Table 3
Main features and values assumed for this study.

1	The Sun-Earth-Moon barycenter is at the CM of the Sun.
2	The Sun-Earth-Moon is a closed system, $\sum_{\forall k} \vec{p}_k = 0$.
3	The initial position of vector $\vec{r}_{cl,d}$, which connects the lunar CM with the POI, is assumed to be $\theta_{cl} \approx \theta_{l,0} - 260.69^o$. This value was fitted by comparing the result with the Ephemerides (NASA-JPL, 2021)[10].
4	The obliquity to the ecliptic, ϕ_{cn}, is assumed constant during the whole axial precession period.
5	It is assumed that ω_{pres} is constant in the whole precession period.
6	The initial θ_{cn} is assumed to be $\theta_{cn,0} \approx 35^o$. This value was fitted by comparing the result with the Ephemerides (NASA-JPL, 2021)[10].
7	The model neglects any relativistic effect.
8	The lunar synodic period (lunar month) is assumed constant.
9	The Sun is assumed to be a disk with a constant average diameter of 0.5329 degrees observed from the Moon.
10	Eclipses with Earth are not considered.
11	No slopes of the terrain are considered.
12	Reflections are assumed negligible.

Table 4
Sites on the lunar south pole with high average solar illumination at 10 [m] above the surface level reported by (Mazarico et al., 2011) and adjusted positions. The average illumination, in this study, was estimated by dividing the number of illumination hours, weighted by the visible solar disk unitary area at the POI, by the total number of hours of the data set.

	Mazarico study			This study			
#[1]	Longitude	Latitude	Aver. illum. (%)	Adjusted Longitude	Adjusted Latitude	Aver. illum. (%)	Abs. Error (%)
1	222.69	−89.45	93.10	222.6627	−89.4511	91.80	1.2966
2	222.73	−89.43	92.53	222.6415	−89.4333	85.17	7.3552
3	223.28	−89.44	92.26	222.8084	−89.4390	91.69	0.5738
4	204.27	−89.78	87.41	203.6490	−89.7797	86.67	0.7365
5	203.46	−89.77	87.42	203.2861	−89.7731	84.34	3.0768
6	37.07	−85.30	87.30	37.1013	−85.2963	78.82	8.4826
7	123.64	−88.81	85.59	123.7604	−88.8084	84.77	0.8184
8	197.05	−89.69	85.93	197.1382	−89.6866	85.99	0.0621
9	222.14	−89.44	91.86	222.4191	−89.4407	91.83	0.0346
10	37.01	−85.30	87.33	37.0207	−85.2897	82.43	4.9033
11	291.90	−88.67	84.74	291.7803	−88.6704	85.98	1.2417
12	198.43	−89.69	85.19	197.7447	−89.6884	80.10	5.0864
13	202.69	−89.76	86.88	202.8645	−89.7624	82.28	4.5985
14	222.59	−89.47	89.57	222.5634	−89.4734	87.94	1.6326
15	223.25	−89.45	91.82	222.7638	−89.4502	91.91	0.0911
16	291.58	−88.68	84.68	291.5466	−88.6782	84.33	0.3542
17	205.14	−89.79	86.19	203.8539	−89.7880	81.74	4.4464
18	37.57	−85.55	82.62	37.5851	−85.5405	75.23	7.3872
19	123.95	−88.80	84.92	123.9526	−88.8025	67.58	17.3354
20	31.73	−85.43	83.32	31.7488	−85.4099	83.59	0.2728

1: This column provides the number of each site in the order they appear on Mazarico report, but they do not correspond necessarily to the single most illuminated 20 locations at 10 m above the lunar soil. Please refer to (Mazarico et al., 2011).

Fig. 8 shows the results for Site 16. As observed, the absolute error is always less than 0.5°, which is comparable to the diameter of the Sun observed from Earth-Moon (0.5329 degrees, see Table 3). The linear increment of the error is mainly due to the accumulation of error in each time-step by the Euler approximation used to solve the three-body problem. Therefore, the linear increment of the error can be reduced by implementing other more efficient numerical algorithms, *e.g. Runge Kutta fourth order*.

The system is assumed to be initially in the arrangement of Fig. 9, based on the data provided by the Ephemerides HORIZONS Web-Inteface (NASA-JPL, 2021)[10] for the period from 06-July-2023 to 14-Feb-2042, which corresponds to a whole APC. Such a period is selected for the proximity to the Aphelion of year 2023 before the long stay of NASA's Artemis base camp. Thus, the initial vectors of position and velocities of each body can be expressed from Fig. 9 as

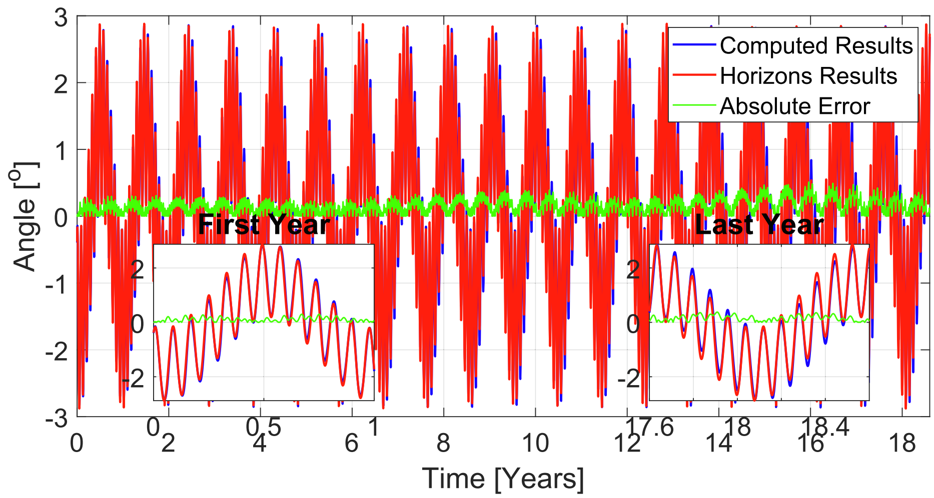

Fig. 8. Solar elevation angle for a whole APC computed by the model presented in Section 3 and Horizons System results of the JPL of NASA and the absolute error between the two models for Site 16. The APC corresponds to the period from 06-July-2023 to 14-Feb-2042. The left inset corresponds to a zoom into the first year while the right inset belongs to the last year of the APC.

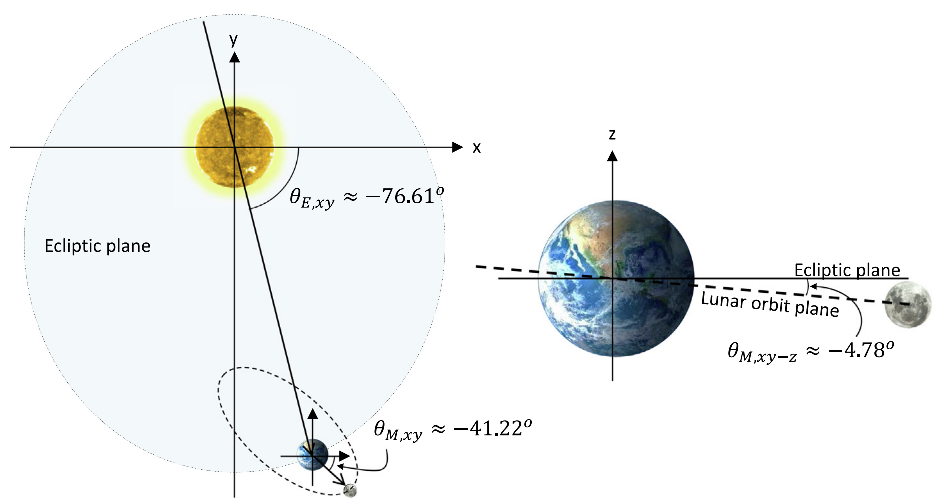

Fig. 9. Initial condition of the Sun-Earth-Moon system at 00 h Universal Time, 06-July-2023, observed from the celestial north. The system is roughly at the Aphelion for the Earth and Perigee for the Moon. The celestial bodies rotate counterclockwise in their own axis and around the parent body. The figure is not drawn to scale.

$$\vec{R}_{SM,0} = R_{SM,x,0}\hat{i} + R_{SM,y,0}\hat{j} + R_{SM,z,0}\hat{k}, \tag{27}$$

$$\begin{aligned} R_{SM,x,0} &= \left|\vec{R}^{max}_{SE}\right| \cos\theta_{E,xy} + \left|\vec{R}^{min}_{EM}\right| \cos\theta_{M,xy-z}\cos\theta_{M,xy}, \\ R_{SM,y,0} &= \left|\vec{R}^{max}_{SE}\right| \sin\theta_{E,xy} + \left|\vec{R}^{min}_{EM}\right| \cos\theta_{M,xy-z}\sin\theta_{M,xy}, \\ R_{SM,z,0} &= \left|\vec{R}^{min}_{EM}\right| \sin\theta_{M,xy-z}, \\ \vec{R}_{SE,0} &= R_{SE,x,0}\hat{i} + R_{SE,y,0}\hat{j} + R_{SE,z,0}\hat{k}, \\ R_{SE,x,0} &= \left|\vec{R}^{max}_{SE}\right| \cos\theta_{E,xy}, \\ R_{SE,y,0} &= \left|\vec{R}^{max}_{SE}\right| \sin\theta_{E,xy}, \\ R_{SE,z,0} &= 0, \end{aligned} \tag{28}$$

where the angles are described in Fig. 9 while $\vec{R}^{max}_{SE}$ and $\vec{R}^{min}_{EM}$ represent the Aphelion and Perigee provided in Table 2. The initial velocities are expressed as

$$\begin{aligned} \vec{v}_{SM,0} &= v_{SM,x,0}\hat{i} + v_{SM,y,0}\hat{j} + v_{SM,z,0}\hat{k}, \\ v_{SM,x,0} &= v_{SE,x,0} - \left|\vec{v}^{max}_{EM}\right| \sin\theta_{M,xy}, \\ v_{SM,y,0} &= v_{SE,y,0} + \left|\vec{v}^{max}_{EM}\right| \cos\theta_{M,xy}, \\ v_{SM,z,0} &= v_{SE,z,0}, \end{aligned} \tag{29}$$

$$\begin{aligned} \vec{v}_{SE,0} &= v_{SE,x,0}\hat{i} + v_{SE,y,0}\hat{j} + v_{SE,z,0}\hat{k}, \\ v_{SE,x,0} &= -\left|\vec{v}^{min}_{SE}\right| \sin\theta_{E,xy}, \\ v_{SE,y,0} &= \left|\vec{v}^{min}_{SE}\right| \cos\theta_{E,xy}, \\ v_{SE,z,0} &= 0, \end{aligned} \tag{30}$$

where $\overrightarrow{v}_{SE}^{min}$ is the minimum orbital velocity of the Earth with respect to the Sun and $\overrightarrow{v}_{EM}^{max}$ is the maximum orbital velocity of the Moon with respect to the Earth, see Table 2.

For this study, the time-series illumination profile of a single site was assumed to be the portion of the visible unitary area of the solar disk from the POI. The positions of the Sun in the lunar sky for two consecutive hours have a separation larger than the average radius of the solar disk. Therefore, the estimation of the visible unitary area, A_{pu}, of the solar disk from the POI can be computed each hour as follows,

$$A = R_s^2\left[\frac{\pi}{2} - \arccos\left(\frac{a}{R_s}\right)\right] + \frac{R_s^2}{2}\sin\left[2\arccos\left(\frac{a}{R_s}\right)\right] - 2ha, \quad (31)$$
$$a = \sqrt{R_s^2 - h^2},$$
$$A_{pu} = \frac{A}{\pi R_s^2},$$

where R_s is the average radius of the solar disk observed from the Moon and $h = \beta_{crit} - \theta_e$ at each hour, see Table 3. The results for sites 1 and 20 are illustrated in Fig. 10 and Fig. 11, respectively. Both the terrain and Sun elevation profiles start in the direction of the Sun with respect to the Moon on July 6, 2023, approximately 103.4688^o, see Fig. 9.

The WLD of a group of sites corresponds to the day with the worst conditions according to the strategy presented in the following sections.

5. Selection of the optimal sites

A suitable location upon the Moon surface for a lunar base is specified by different factors, where the available energy is of paramount importance. For a PV-based lunar station, the availability of sunlight is vital. However, the lunar terrain is highly irregular, which may significantly impact the energy availability due to the shadows cast over the POI. Establishing a distributed site is a potential solution to increase the amount of available energy while reducing the darkness periods. In this respect, it is proposed in this paper to harvest the solar energy from different sites with diverse illumination profiles to reduce the longest night time and accordingly increase the energy availability while considering the shortest possible distance among the sites. The illumination condition for a group of sites is computed by the logical function OR, where the inputs are the binary time-series illumination profiles of each site with state true for illuminated (any value above 0 is assumed to be true) and false for darkness. In this paper, the adjusted sites described in Table 4 are used, but the technique is not limited to these few locations. The effectiveness of the proposed technique can be improved by increasing the number and variety of sites. The site locating problem is formulated as an optimization problem with the following objective function (OF). The

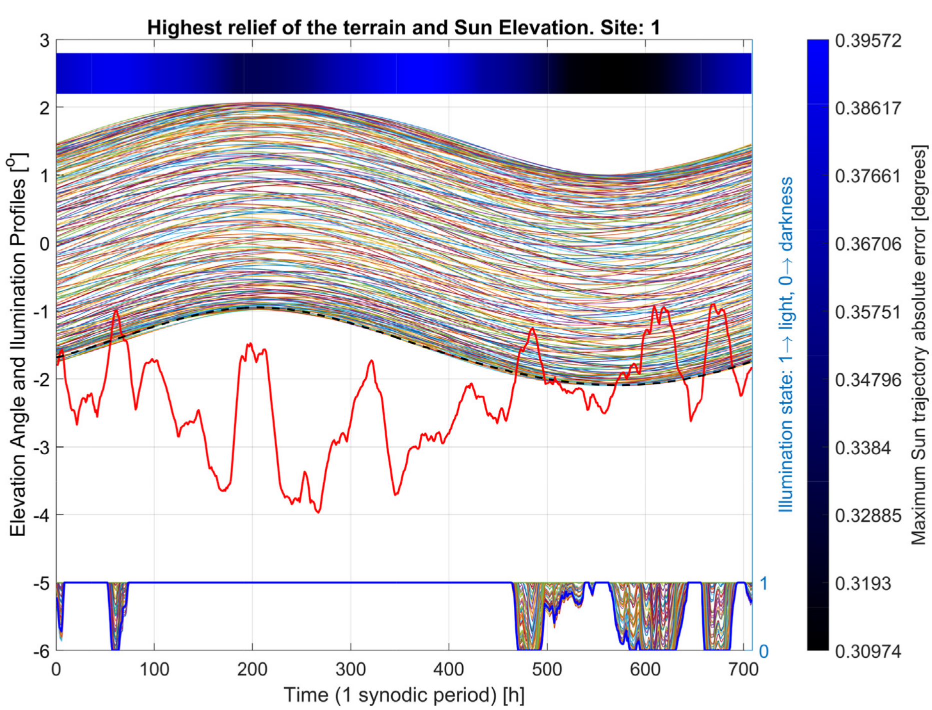

Fig. 10. Time-series illumination profile of Site 1 with a height of 100 [m] upon the lunar terrain. The Sun trajectory corresponds to the whole APC where the trajectory for the WLD is highlighted by a dashed thick line. The terrain elevation around the POI (360°) is represented by the red thick curve while the illumination profile of each day is provided at the bottom. The illumination profile of the WLD is emphasized in blue at the bottom and its y-axis is at the right. The upper colorbar provides the maximum absolute error, in degrees, of the Sun's trajectory (center of the solar disk). observed from the POI with respect to the trajectory estimated by Horizons system of NASA.

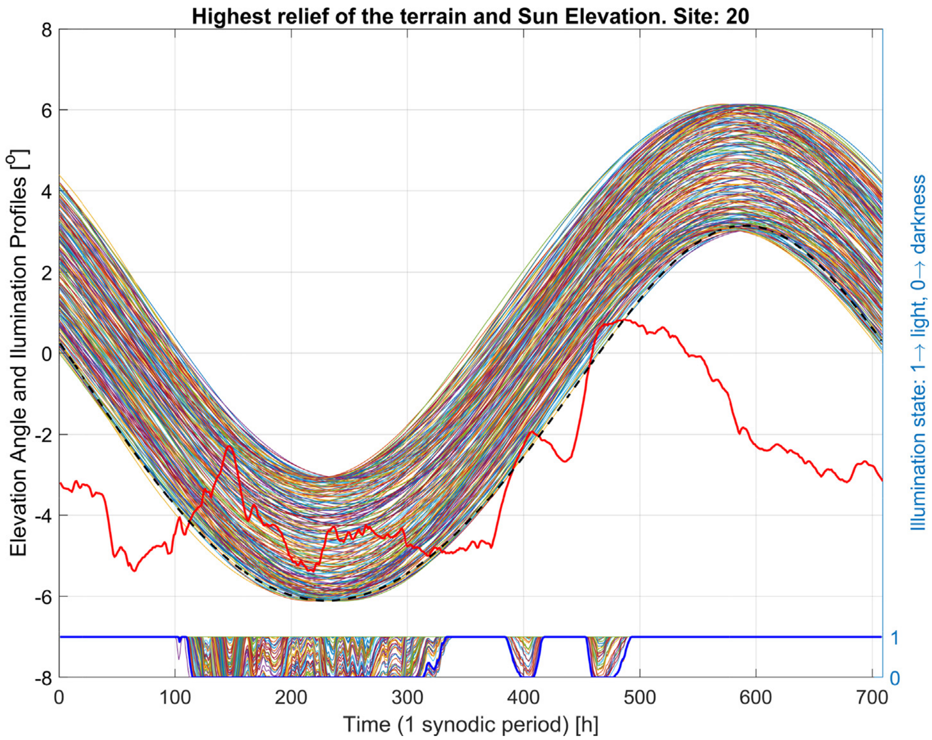

Fig. 11. Time-series illumination profile of Site 20 with a height of 100 [m] upon the lunar terrain. The Sun trajectory corresponds to the whole APC where the trajectory for the WLD is highlighted by a dashed thick line. The terrain elevation around the POI (360°) is represented by the red thick curve while the illumination profile of each day is provided at the bottom. The illumination profile of the WLD is shown in blue and its y-axis is at the right.

Particle Swarm Optimization (PSO) algorithm is used to find the solution.

$$OF = a\frac{N_h - N_{h,min}}{N_{h,max} - N_{h,min}} + b\frac{L - L_{min}}{L_{max} - L_{min}}. \quad (32)$$

In (32), a and b are the weight factors having the condition of $a + b = 1$. The term N_h is the longest night period in the whole APC and L is the total *great-circle length* of a ring connecting all the sites together upon a sphere having the Moon radius (it should be noticed that this distance does not represent the distance of cables that might be required to electrically interconnect the sites. Such a distance would be much longer depending on the terrain shape and drivable path to deploy such a power cable.), R. The ring configuration is intended to increase the RRROS of the system. $N_{h,max}$ and $N_{h,min}$ correspond to the longest and shortest possible night periods in the whole APC independent of the number of selected sites. L_{max} and L_{min} are the maximum and minimum of the total possible length of the ring joining the selected sites. For this study, these values were estimated to be $N_{h,max} = 83$ $[h], N_{h,min} = 0$ $[h], L_{max} = 342.15$ $[km]$, and $L_{min} = 0$ $[km]$.

The goal is to select 1, 2, 3, 4, 5, and 6 sites with different tower heights of 10, 100, and 500 [m] for installation of the PV system. Because the Moon's gravity is approximately 16.6% of the terrestrial gravity and there is no wind loading on the Moon, towers on Moon supporting the same mass should have less weight than ones on Earth with similar height. The decision vector contains the ID number of the candidate adjusted-sites, see Table 4. Different weight factors are tried to explore the Pareto front. The results are provided in the following section.

6. Results

The weighting coefficients a and b in (32) are changed in steps of 0.1 from 0.1 to 0.9. The goal is to find a suitable trade-off between the longest darkness period and the total length of a ring connecting all the selected adjusted-sites. A summary of the results is presented in Table 5.

From Table 5, it is observed that by using more than a single site, it is possible to reduce the number of darkness hours, which would reduce the required ESS size. For the case of PV-modules installed on towers with a height of 10 $[m]$, the best single position is obtained at Site 4 with a longest night of 64 $[h]$. At a total distance of about 316.2 $[km]$ in ring topology or a distance of 158.1 $[km]$ for radial topology, the configuration of two sites can reduce the longest night down to 2 $[h]$. The need for any ESS is removed in configurations comprising more than two sites. When the PV-modules are installed on 100 $[m]$-tall towers above the lunar surface, the longest night for Site 3 is about 36 $[h]$. The need for ESSs can be eliminated by using more than one site. For instance, two sites with 100 $[m]$ tall towers with a separation between sites of 155.85 $[km]$, which results in a distance of 311.7 [km] for the ring configuration, has a longest night of zero hours. At a height of 500 $[m]$, Site 9 was identified as the best option with the

Table 5
Optimal selection of adjusted-sites with the best trade-off between OFs, see (32). The values in the second line of each feature show the result for $a = 0.9$ and $b = 0.1$.. The site configurations with the best compromised solution between OFs, the shortest longest-night with distance zero, and the smallest total-length with 0 h of night are in bold, see Fig. 12.

			Tower height = 10 $[m]$			
No. of sites	One	Two	Three	Four	Five	Six
Arrangement	4	$1 \rightarrow 12$	$13 \rightarrow 14 \rightarrow 16$	$5 \rightarrow 8 \rightarrow 14 \rightarrow 16$	$5 \rightarrow 13 \rightarrow 8 \rightarrow 14 \rightarrow 16$	$13 \rightarrow 12 \rightarrow 8 \rightarrow 14 \rightarrow 16 \rightarrow 5$
of sites[1]	-	$11 \rightarrow 6$	**$14 \rightarrow 16 \rightarrow 7$**	$7 \rightarrow 14 \rightarrow 16 \rightarrow 17$	$14 \rightarrow 16 \rightarrow 4 \rightarrow 5 \rightarrow 7$	$4 \rightarrow 17 \rightarrow 16 \rightarrow 14 \rightarrow 7 \rightarrow 5$
Longest	64	34	8	6	6	6
night $[h]$	-	2	**0**	0	0	0
Shortest	1	1	1	2	2	2
day $[h]$	-	235	**C.I.**	C.I.	C.I.	C.I.
Total	0	18	87.5	89.1	89.1	89.1
distance[2] $[km]$	-	316.2	**154.9**	155	155.2	155.4
			Tower height = 100 $[m]$			
No. of sites	One	Two	Three	Four	Five	Six
Arrangement	3	$3 \rightarrow 16$	$3 \rightarrow 12 \rightarrow 16$	$13 \rightarrow 16 \rightarrow 14 \rightarrow 12$	$13 \rightarrow 12 \rightarrow 8 \rightarrow 14 \rightarrow 16$	$5 \rightarrow 4 \rightarrow 16 \rightarrow 14 \rightarrow 12 \rightarrow 13$
of sites[1]	-	$9 \rightarrow 20$	$16 \rightarrow 7 \rightarrow 14$	$7 \rightarrow 17 \rightarrow 16 \rightarrow 14$	$16 \rightarrow 4 \rightarrow 5 \rightarrow 7 \rightarrow 14$	$17 \rightarrow 16 \rightarrow 14 \rightarrow 7 \rightarrow 5 \rightarrow 4$
Longest	36	15	7	6	6	6
night $[h]$	-	0	0	0	0	0
Shortest	1	1	1	8	8	8
day $[h]$	-	C.I.	C.I.	C.I.	C.I.	C.I.
Total	0	74.8	88.5	88.7	88.9	89.1
distance[2] $[km]$	-	311.7	154.9	155	155.2	155.4
			Tower height = 500 $[m]$			
No. of sites	One	Two	Three	Four	Five	Six
Arrangement	**9**	**$11 \rightarrow 9$**	$16 \rightarrow 9 \rightarrow 11$	$3 \rightarrow 16 \rightarrow 11 \rightarrow 9$	$9 \rightarrow 2 \rightarrow 16 \rightarrow 11 \rightarrow 3$	$1 \rightarrow 15 \rightarrow 11 \rightarrow 16 \rightarrow 3 \rightarrow 9$
of sites[1]	-	**$12 \rightarrow 11$**	$16 \rightarrow 14 \rightarrow 7$	$17 \rightarrow 7 \rightarrow 14 \rightarrow 16$	$14 \rightarrow 16 \rightarrow 4 \rightarrow 5 \rightarrow 7$	$14 \rightarrow 16 \rightarrow 17 \rightarrow 4 \rightarrow 5 \rightarrow 7$
Longest	**34**	**6**	6	6	6	6
night $[h]$	-	**3**	0	0	0	0
Shortest	**1**	**596**	596	596	596	596
day $[h]$	-	**30**	C.I.	C.I.	C.I.	C.I.
Total	**0**	**75.6**	75.6	75.6	75.8	75.9
distance[2] $[km]$	-	**84.1**	154.9	155	155.2	155.4

[1] The arrows indicate the order in which the sites (the site IDs are introduced in Table 4) should be connected to get the total distance specified for each site. The last site is connected back to the first site.
[2] This value corresponds to a ring configuration connecting all the sites together. C.I.: Continuous illumination.

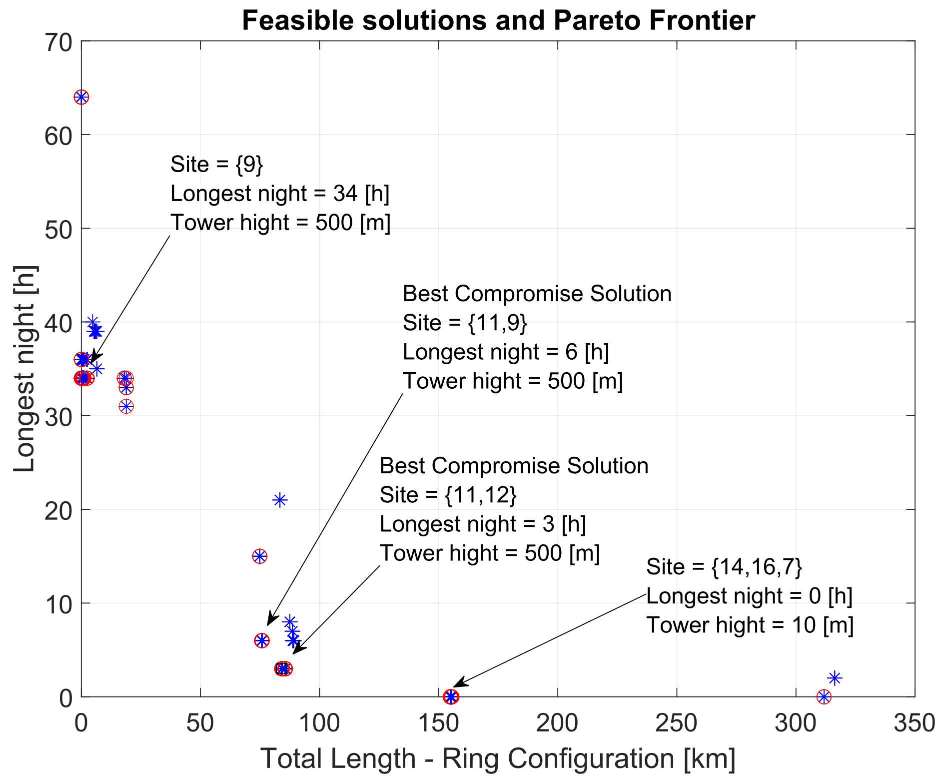

Fig. 12. Candidate configurations, Pareto front (red circles), and the best compromise solution (See bold parts in Table 5).

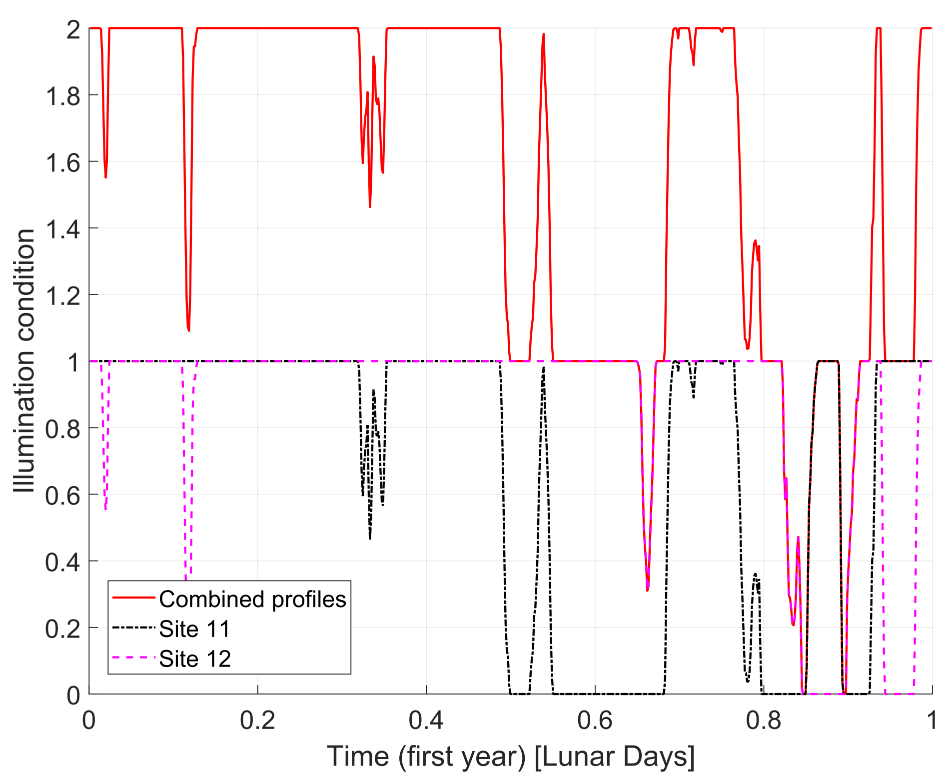

Fig. 13. Illumination time-series profiles of sites 11 and 12 and their combination. Zero indicates darkness, 1 means that one site is fully illuminated while the other is in darkness, and 2 means that both sites are fully illuminated.

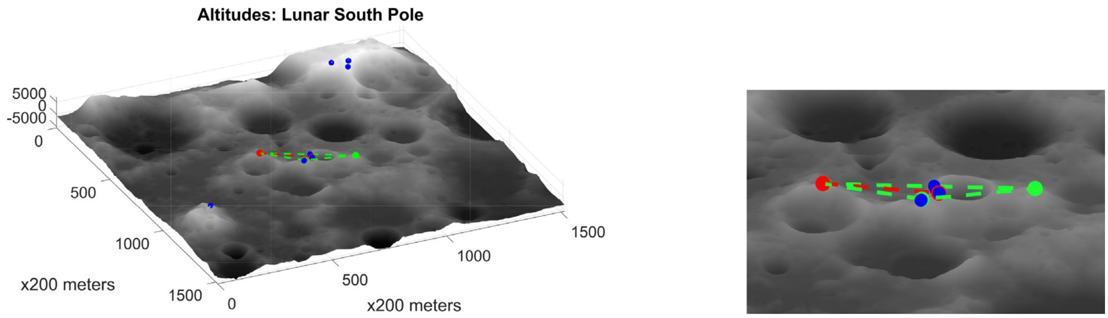

Fig. 14. Graphical representation of the best compromise solution (sites 11 and 12) by the dashed red line and a configuration of three sites to prevent the use of ESS by the dashed green line (sites 7, 14, and 16). Right figure: zooming of the best compromised solutions.

shortest longest-night period of 34 [h]. For that tower height, the use of ESSs can be omitted by selecting more than two sites. It should be noticed that the optimization algorithm identifies the sites 12 and 11 as the best configuration when $a = 0.9$ and $b = 0.1$ upon the configuration comprised of the sites 9 and 20 because the much shorter distance of separation.

For the final selection of a suitable configuration for different number of sites and tower heights, the Pareto front is identified using the OF given in (32). Fig. 12 shows the candidate solutions of the problem, where the Pareto front is represented by red circles. The best compromise solution is proposed to be found with the well-known membership approximation technique assuming a weight factor of 30% for the total length and 70% for the longest night. According to the results and considering just the 20 adjusted-sites listed in Table 4, the best compromise solution is obtained at a tower height of 500 [m] in two sites 11 and 12, with a distance of approximately 42.05 [km] between the sites. Such a configuration does not eliminate the need of ESS, but reduces the required ESS size by decreasing the length of the longest night down to 3 [h]. A three-site configuration with towers of 10 [m] (sites 14, 16, and 7) avoids the use of ESSs since the combination keeps at least one of the sites illuminated (please, refer to Table 3 to see the assumptions considered for this study). Fig. 13 shows the illumination time-series profiles of sites 11 and 12 and the combined illumination profile for the first lunar day. The combined profile goes from zero up to two. Zero means darkness in both sites, one means that the resultant illumination in both sites corresponds to one site fully illuminated, and two means that both sites are fully illuminated. Fig. 14 shows a graphical representation of two configurations upon the lunar south pole. The optimal best compromise solution (sites 11 and 12) is shown by a dashed red line, while the configuration to avoid the need of any ESS is represented by a dashed green line. Fig. 15 shows the algorithm followed to compute the time-series illumination profiles.

7. Conclusion

This paper has proposed a novel technique to estimate the Sun illumination availability for a configuration of more than one PV-based site in the lunar south pole region. The proposed technique is based on a new method to estimate the critical elevation angles and the Sun position in the Moon's sky by means of analytical models that are solved numerically. The proposed technique is suitable for engineering applications that aim to estimate the Sun availability in different sites for a variety of purposes such as base planning and operation management. The results have shown good accuracy for estimation of Sun trajectories as well as availability of Sun illumination in the studied locations compared to the previously reported studies. Furthermore, the individual time-series illumination profiles were combined into different arrangements of 1, 2, 3, 4, 5, and 6 sites aiming to find the optimal configuration. The goal was to minimize the longest darkness time while keeping the shortest possible total distance between the sites. The Pareto front was computed by the PSO algorithm with the whole APC as the optimization horizon. The PV modules were assumed to be at elevations of 10, 100, and 500 [m] above the lunar surface. The results showed that the best compromise multi-site configuration, which reduces the length of the longest night down to 3 [h], is comprised of the sites 11 (longitude 291.7803° and latitude −88.6704°) and 12 (longitude 197.7447° and latitude −89.6884°). In that configuration, the PV modules are at a height of 500 [m], with a separation of approximately 42.05 [km] between the sites. Another solution suggests a three-site configuration (7, 14, and 16) that can prevent the use of any ESS with PV modules on 10 [m]-tall towers, but would require a separation of about 154.9 [km] in ring configuration (some ESS would be needed for the solar eclipses by the Earth). More interesting arrangements were provided with the longest nights shorter than 10 [h], which can also be very promising for future lunar SMGs. Even when the separation between the sites of these compromise

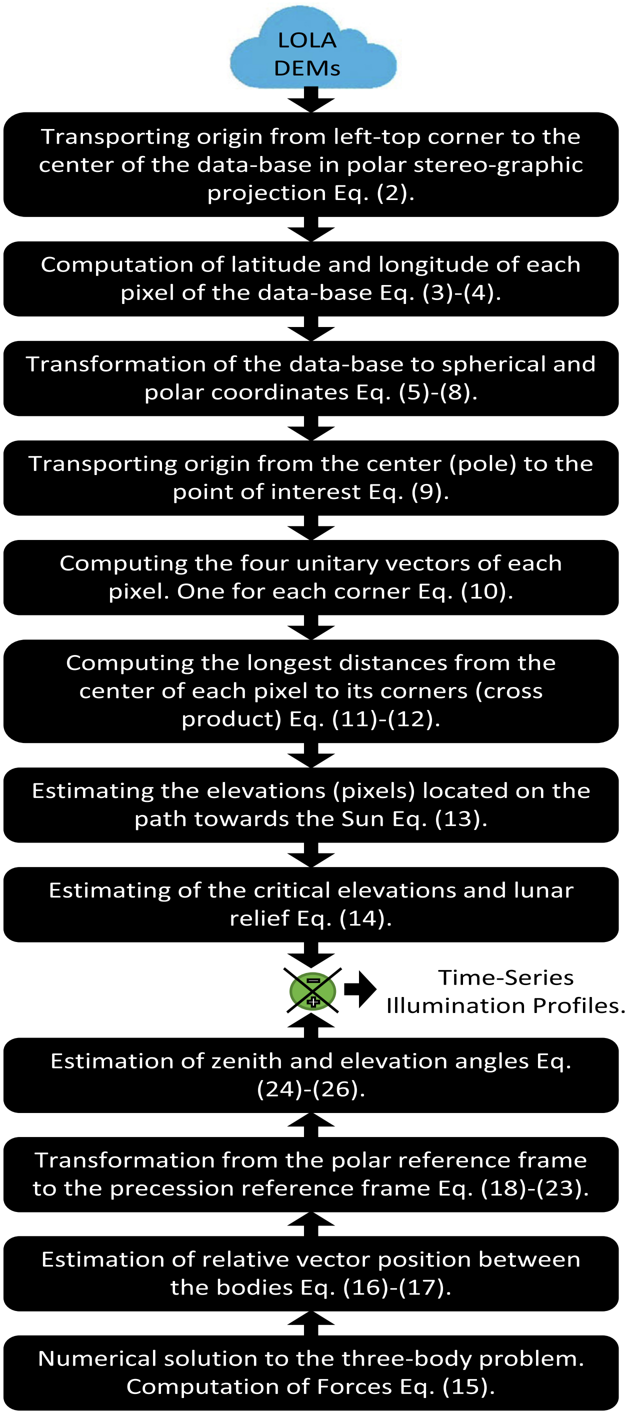

Fig. 15. Algorithm to compute the time-series illumination profiles.

solutions is in the range of kilometers, the experience during simulations showed that it might be possible to get better compromise solutions, which would have shorter distances between the sites while having shorter or similar night-times to the current solutions found in this study. This might be feasible by increasing the number of potential sites to be considered in the optimization problem and by testing different tower heights at different places. In this study, it is assumed that all the locations in the same potential compromise solution have the same tower heights. For instance, for a configuration of three sites, one site could have a 10 meter tower, while the others 100 meter tower. However, since a population-based algorithm is used to solve the optimization problem, the increase of degrees of freedom would either increase the processing time[2] to get the solutions or reduce the ratio of exploration of the particles in the searching space, depending on the chosen termination criterion. For distances in the range of multiple 10's km, laser beamed power transmission technologies may be considered for transmission of power between the sites without the need for long power cables. Nevertheless, more work is needed regarding laser power beaming since this technology has low efficiency with the need of heavy auxiliary systems (like thermal systems). On the other hand, power cables could be applicable to hazardous lunar conditions depending on the outcome of future technology development. However, the laying of cables on the lunar terrain and through such distances would be itself a paramount challenge.

The current study takes into consideration, for optimization purposes, only the distance between the sites and the longest night time, which will affect the ESS sizing. However, more factors should be considered to increase the validity of the results. One important factor is the expected energy and power demanded by the lunar base throughout the mission duration, which will allow to estimate the size and weight of the power system at each site. This in turn will provide the data required to estimate the cost of power generation and transmission.

Declaration of Competing Interest

The authors declare that they have no known competing financial interests or personal relationships that could have appeared to influence the work reported in this paper.

Acknowledgment

This work was supported by the Mexican National Council of Science and Technology (CONACYT) [scholarship number 709940]; the research work was funded also by a Villum Investigator grant (No. 25920) from The Villum Fonden; and partly sponsored by the Universidad de la Salle Bajío, Guanajuato, México.

Appendix A. Supplementary material

Supplementary data associated with this article can be found, in the online version, at https://doi.org/10.1016/j.asr.2022.12.048.

[2] The processing time will depend on several factors, such as the number of particles chosen for the population-based algorithm, the coding of the algorithm, the characteristics of the processor, *etc.*.

References

Barker, M.K., Mazarico, E., Neumann, G.A., Smith, D.E., Zuber, M.T., Head, J.W., 2021. Improved LOLA elevation maps for south pole landing sites: Error estimates and their impact on illumination conditions. Planet. Space Sci. 203, 105119. https://doi.org/10.1016/j.pss.2020.105119.

Bukszpan, D., 2020. Why NASA wants to put a nuclear power plant on the moon. URL: https://www.cnbc.com/2020/11/15/why-nasa-wants-to-put-a-nuclear-power-plant-on-the-moon.html. (Accessed on 23/07/2022).

Bussey, D.B.J., Spudis, P.D., Robinson, M.S., 1999. Illumination conditions at the lunar South Pole. Geophys. Res. Lett. 26, 1187–1190. https://doi.org/10.1029/1999GL900213.

Choi, S.H., King, G.C., Kim, H.J., Park, Y., 2010. Electrostatic Power Generation from Negatively Charged, Simulated Lunar Regolith. AIAA SPACE URL: https://ntrs.nasa.gov/citations/20100032922.

Colozza, A.J., 2020. Small Lunar Base Camp and In Situ Resource Utilization Oxygen Production Facility Power System Comparison. Technical Report NASA/CR—2020-220368. National Aeronautics and Space Administration (NASA). URL: https://ntrs.nasa.gov/citations/20200001622.

Dunbar, B., 2021. NASA artemis. URL: https://www.nasa.gov/specials/artemis/. (Accessed on 10/14/2021).

Fincannon, H.J., 2020. Lunar Environment and Lunar Power Needs. Springer Handbook Series Contribution. pp. 1–5. URL: https://ntrs.nasa.gov/citations/20205002224.

Fincannon, J., 2007. Lunar South Pole Illumination: Review, Reassessment, and Power System Implications. American Institute of Aeronautics and Astronautics. pp. 1–24. https://doi.org/10.2514/6.2007-4700.

Fincannon, J., 2008a. Characterization of Lunar Polar Illumination from a Power System Perspective. American Institute of Aeronautics and Astronautics. pp. 1–50. https://doi.org/10.2514/6.2008-447.

Fincannon, J., 2008b. Lunar Polar Illumination for Power Analysis. American Institute of Aeronautics and Astronautics. pp. 1–20. https://doi.org/10.2514/6.2008-5631.

Freeh, J., 2009. Analysis of stationary, photovoltaic-based surface power system designs at the lunar south pole. In: AIAA SPACE 2008 Conference & Exposition, p. 7810. URL: https://ntrs.nasa.gov/citations/20090015377.

Gibson, M., Schmitz, P., 2020. Higher power design concepts for nasa's kilopower reactor. In: 2020 IEEE Aerospace Conference, IEEE. pp. 1–9. https://doi.org/10.1109/AERO47225.2020.9172530.

JAXA, 2019. The jaxa space exploration innovation hub center co-produces results on remote and automatic control to build lunar base. URL: https://global.jaxa.jp/press/2019/03/20190328a.html. (Accessed on 10/14/2021).

Jin, K., Zhou, W., 2019. Wireless laser power transmission: A review of recent progress. IEEE Trans. Power Electron. 34, 3842–3859. https://doi.org/10.1109/TPEL.2018.2853156.

Kerslake, T.W., 2008. Lunar surface-to-surface power transfer. AIP Conf. Proc. 969, 466–473. URL: https://aip.scitation.org/doi/abs/10.1063/1.2845004 , https://doi.org/10.1063/1.2845004. Complete report: https://ntrs.nasa.gov/citations/20080008842.

Li, X., Wang, S., Zheng, Y., Cheng, A., 2008. Estimation of solar illumination on the moon: A theoretical model. Planet. Space Sci. 56, 947–950. https://doi.org/10.1016/j.pss.2008.02.008.

Lisbona, E.F., 2005. llf-2 - calibration, testing and monitoring of space solar cells. In: Markvart, T., Castañer, L. (Eds.), Solar Cells. Elsevier Science, Oxford, pp. 475–503. https://doi.org/10.1016/B978-185617457-2/50019-6.

Masayuki, N., Nobuyuki, H., Mana, S., Yoshiharu, A., Junichi, H., Matias, L.J.A., Ja, K.K., Satoshi, K., 2020. Radiation dose and its protection in the Moon from galactic cosmic rays and solar energetic particles: at the lunar surface and in a lava tube. J. Radiol. Prot. 40, 947–961. https://doi.org/10.1088/1361-6498/abb120.

Mazarico, E., Neumann, G., Smith, D., Zuber, M., Torrence, M., 2011. Illumination conditions of the lunar polar regions using LOLA topography. Icarus 211, 1066–1081. https://doi.org/10.1016/j.icarus.2010.10.030.

NASA, 2020. PDS Geosciences Node Data and Services: LRO LOLA. URL: https://pds-geosciences.wustl.edu/missions/lro/lola.htm. (Accessed on 01/12/2020).

NASA-JPL, 2021. Solar System Dynamics: HORIZONS Web-Interface. URL: https://ssd.jpl.nasa.gov/horizons/app.html#/. (Accessed on 01/09/2021).

Neumann, G., Smith, D., Scott, S., Slavney, S., Grayzek, E., 2016. Lunar Reconnaissance Orbiter Lunar Orbiter Laser Altimeter reduced data record and derived products software interface specification, version 2.6. National Aeronautics and Space Administration Planetary Data System (Accessed 01 December 2020) URL: http://pds-geosciences.wustl.edu/missions/lro/lola.htm.

Noda, H., Araki, H., Goossens, S., Ishihara, Y., Matsumoto, K., Tazawa, S., Kawano, N., Sasaki, S., 2008. Illumination conditions at the lunar polar regions by kaguya (selene) laser altimeter. Geophys. Res. Lett. 35. https://doi.org/10.1029/2008GL035692.

Peng, C., Ding, F., Lei, Z., Zhang, Z., En, Y., Huang, Y., 2020. Investigation of radiation-induced degradations in four-junction solar cell by experiment and simulation. Microelectron. Reliab. 108, 113646. https://doi.org/10.1016/j.microrel.2020.113646.

Raya-Armenta, J.M., Bazmohammadi, N., Vasquez, J.C., Guerrero, J.M., 2021. A short review of radiation-induced degradation of III–V photovoltaic cells for space applications. Sol. Energy Mater. Sol. Cells 233, 111379. https://doi.org/10.1016/j.solmat.2021.111379.

Smith, D.E., Zuber, M.T., Jackson, G.B., Cavanaugh, J.F., Neumann, G.A., Riris, H., Sun, X., Zellar, R.S., Coltharp, C., Connelly, J., et al., 2010a. The lunar orbiter laser altimeter investigation on the lunar reconnaissance orbiter mission. Space Sci. Rev. 150, 209–241. https://doi.org/10.1007/s11214-009-9512-y.

Smith, D.E., Zuber, M.T., Neumann, G.A., Lemoine, F.G., Mazarico, E., Torrence, M.H., McGarry, J.F., Rowlands, D.D., Head III, J.W., Duxbury, T.H., Aharonson, O., Lucey, P.G., Robinson, M.S., Barnouin, O.S., Cavanaugh, J.F., Sun, X., Liiva, P., Mao, D.d., Smith, J.C., Bartels, A.E., 2010b. Initial observations from the Lunar Orbiter Laser Altimeter (LOLA). Geophys. Res. Lett. 37. https://doi.org/10.1029/2010GL043751.

Speyerer, E.J., Robinson, M.S., 2013. Persistently illuminated regions at the lunar poles: Ideal sites for future exploration. Icarus 222, 122–136. https://doi.org/10.1016/j.icarus.2012.10.010.

Summerer, L., Purcell, O., 2009. Concepts for wireless energy transmission via laser. URL: https://www.esa.int/gsp/ACT/doc/POW/ACT-RPR-NRG-2009-SPS-ICSOS-concepts-for-laser-WPT.pdf.

Williams, D.R., 2018. Sun Fact Sheet. NASA Goddard Space Flight Center.

Williams, D.R., 2020a. Earth Fact Sheet. NASA Goddard Space Flight Center.

Williams, D.R., 2020b. Moon Fact Sheet. NASA Goddard Space Flight Center.